JOURNAL OF THERMOPHYSICS AND HEAT TRANSFER
Vol. 21, No. 1, January–March 2007

Computational Simulation of High-Enthalpy Arc Heater Flows

Takeharu Sakai*
Nagoya University, Nagoya 464-8613, Japan

DOI: 10.2514/1.26083

The flowfields in segmented constrictor-type arc heaters are simulated using a new Navier–Stokes code named ARCFLO3. The validity of the radiation and turbulence modeling employed in ARCFLO3 is assessed by comparing the calculated results with the existing experimental data obtained in the 20 and 60 MW arcjet facilities at NASA Ames Research Center. Comparison is made between the calculated and the measured data for arc voltage, heater efficiency, mass-averaged enthalpy, chamber pressure, heat flux at wall, and total enthalpy in the centerline region of an arcjet flow. The results show a good agreement for the 60 MW facility but a relatively poor agreement for the 20 MW facility. A possible reason for the discrepancy is given.

Nomenclature

A_{th}	=	throat area, m^2
D	=	constrictor diameter, m
H	=	total enthalpy, J/kg
I	=	electrical current, A
L	=	constrictor length, m
$\dot{m}$	=	mass flow rate, kg/s
P	=	heater power, MW
p_{ch}	=	chamber pressure, atm
q	=	heat flux, W/cm^2
R	=	constrictor radius, m
r	=	radial distance, m
T	=	temperature, K
u	=	velocity in x-direction, m/s
V	=	voltage, V
x	=	axial distance, m
η	=	heater efficiency
κ_λ	=	absorption coefficient at given wavelength including stimulated emission, cm^{-1}
ν	=	kinematic viscosity, m^2/s
ρ	=	density, kg/m^3
σ	=	electrical conductivity, mho/m

Subscripts

av	=	mass average
cl	=	centerline
rad	=	radiation
t	=	turbulent

I. Introduction

SEGMENTED constrictor-type arc heaters are used to produce the high-enthalpy flow conditions encountered during the atmospheric entries of space vehicles. The constricted-type arc heater consists of an upstream electrode (anode) chamber, constrictor section, and downstream electrode (cathode) chamber. A schematic diagram of a typical facility is shown in Fig. 1. Flow conditions are adjusted by varying the two control parameters: arc electrical current and test gas mass flow rate. The test gas is injected mainly from the constrictor section and partly from two electrode chambers. The gas is heated by an electric discharge through the arc heater, and is expanded through a nozzle to a test section. In high-power level arc heaters such as the 20 MW Aerodynamic Heating Facility (AHF), the 20 MW Panel Test Facility (PTF) or the 60 MW Interaction Heating Facility (IHF) at NASA Ames Research Center (See Table 1 for operational capabilities) [1], strong radiative and Joule heating occur, and the flow is turbulent in the constrictor.

It is desirable to be able to predict the arc heater flowfield for understanding of the arcjet freestream, design of a new arc heater, or improvement of a heater efficiency. An arc heater flowfield code named ARCFLO had been developed in the 1970s to calculate the constrictor flowfield [2]. The code incorporates a two-band gray-gas radiation model and an eddy-viscosity turbulence model. Recently, a new CFD code named ARCFLO2 that solves the flow from the anode through the nozzle throat has been developed by Kim et al. [3]. The primary objective of [3] was to convert the spatial marching in the previous ARCFLO into time-marching. More recently, the computational algorithms in ARCFLO2 has been improved by the present author and his associates [4] to minimize the numerical instability occurring in simulating high heating conditions. In this latest version, named ARCFLO3, the physical models such as radiation, transport properties, or turbulence are retained from the original ARCFLO code.

In [4], those physical models were shown to be inadequate for accurate predictions of the operational characteristic parameters such as arc voltage, heater thermal efficiency, mass-averaged enthalpy, and chamber pressure for AHF. The present study is a continuation of the previous work [4], and aims to improve the ARCFLO3 code. In this paper, attention is on modifications of the radiation model to be consistent with detailed radiation calculations and the turbulence model. Using both original and modified physical models, computed heat fluxes are compared with the measurement in the PTF arc heater [5] to show the validity of the improved model. The improved ARCFLO3 code is applied to calculate voltage, heater efficiency, mass-averaged enthalpy, chamber pressure and the enthalpy in the centerline region of the arcjet flow for typical AHF and IHF operating conditions. The results are compared with the data from a series of arcjet tests in the AHF [6,7] and the IHF [8].†

The present work shows that a good agreement is obtained between the experiment and calculation for the IHF arc heater conditions, but a poor agreement for the AHF arc heater conditions. A possible cause of the disagreement is offered.

II. Physical and Numerical Modeling

A. Radiation Modeling

1. Brief Review of Earlier Works

Previously, Milos [9] computed the radiative heat fluxes at the wall in a constrictor region by using both a two-band model and a

Presented as Paper 1183 at the Computational Simulation of High Enthalpy Arc Heater Flows, Reno, NV, 9–12 January 2006; received 22 June 2006; revision received 22 August 2006; accepted for publication 20 August 2006.

*Assistant Professor, Department of Aerospace Engineering. Member AIAA.

†T. M. Hightower and J. Balboni, private communication, January 2003.

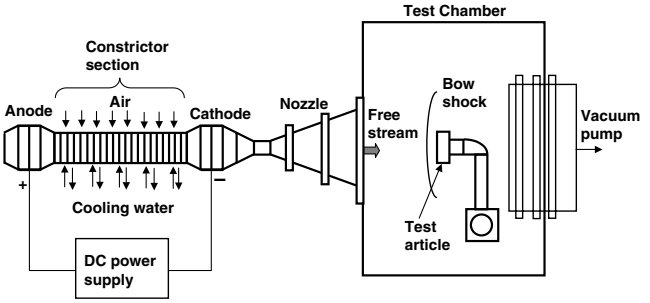

Fig. 1 Schematic diagram of an arcjet facility.

detailed-spectral radiation code, NEQAIR [10]. The comparison showed that the two-band model overestimated the wall radiative heat flux by a factor of 2 as compared to NEQAIR [9]. Taunk et al. [5] measured the total heat flux from the constrictor region of the PTF arc heater. The PTF arcjet facility has a constrictor diameter of 6 cm and length of 2.4 m. A semi-elliptic nozzle was used for the measurement. As shown in Table 1, the main dimensions and power level of the PTF arc heater are almost the same as those of the AHF arc heater. Therefore, the constrictor heating environment for the PTF is expected to be similar to that for the AHF. Calculations were made using the original ARCFLO code and compared with those data [5]. The results showed that the calculation overestimated the measured heat flux in the upstream region and underestimated in the downstream region [5].

In our previous work [4], calculations were made for the different arc heater operating conditions at the mass flow rates ranging from 0.05 to 0.4 kg/s and the electrical currents from 1100 to 2200 A. The computed voltage between the electrodes, mass-averaged enthalpy, and chamber pressure were compared with a set of experimental data [6] obtained in the AHF. The results showed a discrepancy between experiment and calculations [4].

Radiation modeling will strongly affect computed flow properties because of the high temperature in the arc heater. Assuming that the high-fidelity NEQAIR prediction is more accurate, these results suggest that one possible cause of the discrepancy shown in our previous work [4] may be the inaccuracy of the two-band radiation model.

In the present study, the radiative transfer equation in cylindrical coordinates is solved and radiation is calculated in a fully coupled manner with the flow equations. Because the computing time of the line-by-line method is 600 times greater compared to the two-band model, a radiation model with less computing time is desirable for radiation coupled CFD calculations. Attempts have been made to improve the accuracy of the two-band model [9,11]. However, the modified two-band model [9] did not show improvement in the accuracy of the radiative heat flux distribution, and the radiation model developed in the author's past work [11] required a large computing time in the use of the radiation coupled CFD calculation [12]. Therefore, we establish a new method to develop a radiation model compatible with a detailed-spectral radiation model.

2. *New Three-Band Radiation Model*

In this study, a new method is devised based on the Planck–Rosseland–Gray (PRG) model [13]. In the PRG model, an absorption coefficient at a given wavelength and at a given point in a flowfield is classified into one of the Planck, Rosseland, or gray-gas groups based on a local optical depth. In each group, the Planck, Rosseland, or gray-gas approximation [14] is assumed to be valid.

Table 1 Arcjet facilities at NASA Ames Research Center

Facility	P, MW	I, A	$\dot{m}$, kg/s	D, m	L, m	A_{th}, m^2
PTF	20	600–2200	0.05–0.3	0.06	2.4	0.0010
AHF	20	600–2200	0.05–0.4	0.06	2.3	0.0011
IHF	60	2000–6000	0.2–0.7	0.08	3.9	0.0028

The radiative heat fluxes are computed in each group by using wavelength-mean values defined for each group, and the total radiative heat flux is given by a sum of each radiative heat flux. Most of the lines above 2000 Å are classified into the Planck group, and most of the lines below 2000 Å are classified into the Rosseland or gray group.

In the PRG model, the specific selection criteria used to determine into which group a specific wavelength is placed are not known a priori [11,13]. In the new radiation model, the absorption coefficient is classified a priori into one of the three groups: 1) $\kappa_\lambda > a$ cm^{-1} and $\lambda < 2000$ Å; 2) $\kappa_\lambda < a$ cm^{-1} and $\lambda < 2000$ Å; 3) $\lambda > 2000$ Å, where a is a user specified value. In each group, wavelength-mean absorption coefficients are determined by using the so-called escape factor concept. The escape factor ϕ is defined as the probability that a photon emitted at a point will not be absorbed after traveling a distance d by

$$\phi = \frac{\int_0^\infty E_\lambda \exp(-\kappa_\lambda d)\,\mathrm{d}\lambda}{\int_0^\infty E_\lambda\,\mathrm{d}\lambda} \tag{1}$$

where E_λ and κ_λ denote an emission coefficient and an absorption coefficient at a given λ, respectively.

Assuming a wavelength-mean absorption coefficient exists over a certain range, Eq. (1) can be transformed to

$$\kappa = \frac{-\log(\phi)}{d} \tag{2}$$

To obtain the wavelength-mean blackbody (Planck) function, the total specific intensity of radiation, I, is calculated by

$$I = \int_0^\infty I_\lambda\,\mathrm{d}\lambda = \int_0^\infty B_\lambda[1 - \exp(-\kappa_\lambda d)]\,\mathrm{d}\lambda \tag{3}$$

where B_λ denotes the blackbody function at a given λ. In the gray-gas approximation, Eq. (3) becomes

$$I = B[1 - \exp(-\kappa d)] \tag{4}$$

Therefore, by using the κ, d, and I given by Eqs. (2) and (4), the wavelength-mean blackbody function B is given by

$$B = \frac{I}{1 - \exp(-\kappa d)} \tag{5}$$

For a detailed-spectral radiation model, the most recent version of the NEQAIR code [15][‡] is used. The line-by-line method in the NEQAIR code is used to calculate the absorption coefficient of equilibrium air. A Boltzmann distribution of the internal states for air species was used because the gas is assumed to be in equilibrium. The wavelength regions from 650 to 40,000 Å were divided into five regions and 250,000 wavelength points were used. Compared to a result using 900,000 wavelength points, the radiative heat flux reaching to the wall differs by only about 2.5%.

The absorption coefficient criterion a and the characteristic length d are empirically determined to reproduce the radiative heat flux distribution calculated by the line-by-line method for the range of pressures and temperatures occurring in the constrictor region considered in the present study. Two sets of parameters are obtained. For the first set, a is 5 cm^{-1}, $d_1 = d_2 = 2$ cm for $T > 10,000$ K, $d_1 = d_2 = 3$ cm for $T < 10,000$ K and $d_3 = 20$ cm. For the second set, a is 5 cm^{-1}, $d_1 = d_2 = 2$ cm for $T > 11,500$ K, $d_1 = d_2 = 10$ cm for $T < 11,500$ K and $d_3 = 20$ cm. The second set is used only for the case of the IHF conditions at $I = 6000$ A, and all other cases are calculated by the first set. A lookup table of the wavelength-mean values of absorption coefficients and Planck function for the CFD code has been prepared as a function of pressure and temperature over the pressure ranges from 1 to 10 atm and the temperature ranges from 1000 to 15,000 K.

[‡]C. Park, private communication, February 2002.

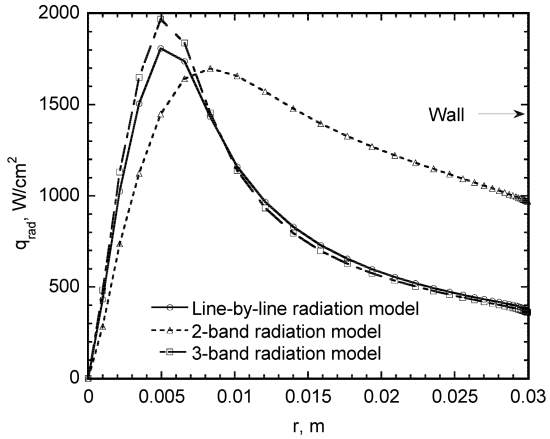

Fig. 2 Comparison of radiative heat flux distribution at constrictor exit between different radiation models.

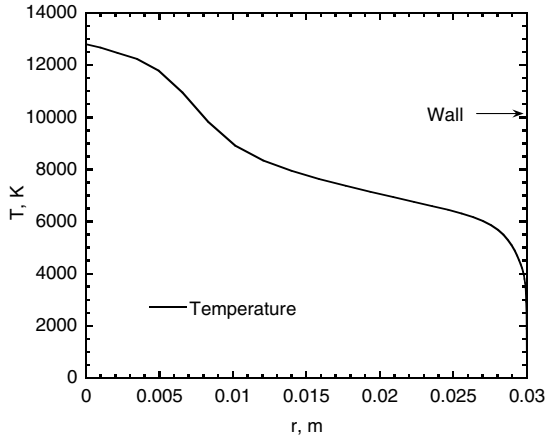

Fig. 3 Temperature distribution at the constrictor exit.

To calculate a radiative heat flux distribution in the radial direction, temperature and pressure profiles are computed by the ARCFLO3 code for the typical case of a mass flow rate of 0.25 kg/s and an electrical current of 2000 A. Figure 2 shows the radial radiative heat flux distributions at the constrictor exit for the line-by-line, the two-band and the new three-band radiation models. The temperature distribution is shown in Fig. 3. The pressure is nearly constant at 5.9 atm. Near the centerline ($r = 0$), radiative heat flux values calculated by the line-by-line model become higher than those obtained by the two-band model. Because the absorption predicted by the two-band model is weak near the wall region, the radiative heat flux reaching the wall calculated by the two-band model is higher than that obtained by the line-by-line model by a factor of 2.

It can be seen also from Fig. 2 that the difference of the radiative heat flux in the core region is 12% and the difference at the wall is less than 1% between the line-by-line and the new three-band radiation models. The three-band model reduces the computing time of the line-by-line model by a factor of 400.

B. Transport Properties

Air, or a mixture of air and argon, is used as the test gas. A set of collision integrals given by the Gupta et al. [16] is used for the collisions including air species. The collision integrals for Ar-N, Ar-O, Ar-N_2, Ar-O_2, Ar-NO, and Ar-Ar are evaluated through a combination rule [17]. For Ar-Ar^+, Ar-e^-, the values given by Devoto [18] are used.

One of the important parameters to calculate the Joule heating in the arc heater flowfield is electrical conductivity. In the original ARCFLO code, the electrical conductivity was determined by the collision integrals $\pi\Omega^{(1,1)}$ for all collision pairs including electron. At temperatures above 12,000 K, which occur at the centerline in the constrictor, the electrical conductivity can be improved by improving the collision integrals for electron-atom pairs. The collision integral data for e-O and e-N collisions given by Gupta et al. were based on the experimental data of total cross sections [16]. For the calculation of the electrical conductivity, we need the momentum cross sections for these collisions.

In our previous work [19], the collision integrals $\pi\Omega^{(1,1)}$ and $\pi\Omega^{(2,2)}$ for e-N and e-O collisions were calculated using the momentum cross sections obtained from the theoretical differential cross sections given by Thomas and Nesbet [20–22] and Blaha and Davis [23]. We assume that $\pi\Omega^{(1,1)} = \pi\Omega^{(2,2)}$. These collision integrals are used in the present study. As was shown in our previous work [19], the calculations using the modified collision integrals give a better comparison of the heat fluxes with the measurement, although the effect of the modified collision integrals were small.

C. Turbulence Modeling

Two eddy-viscosity models for turbulent flow are used in the present study. One is the so-called two-layer model used in the original ARCFLO model and another is the Baldwin–Lomax model [24]. The parameter in the outer layer used in the original ARCFLO model was chosen as to be compatible with the two-band radiation model used. Because the present three-band radiation model gives different emission and absorption characteristics from the two-band radiation model, as was shown in the preceding section, the modeling of convective heat transfer in the ARCFLO3 code may need to be changed.

Calculation has shown that the impact of the turbulence model on the calculated results such as arc voltage, chamber pressure, thermal efficiency, and mass-averaged enthalpy, is not so large in the present calculations. But, the Baldwin–Lomax turbulence model gives a better comparison of the enthalpy in the centerline of the arcjet flow with measurement, as will be shown later.

1. *Original ARCFLO model*

In the eddy-viscosity model in the original ARCFLO code [2], the mixing length is defined differently in the inner near wall region where a wall model is valid, and in the outer core region where the mixing length is assumed to be proportional to the tube radius [2]:

$$l_i = Ky\left\{1 - \exp\left(\frac{-yu_\tau}{26\nu_w}\right)\right\} \tag{6}$$

$$l_o = 0.075R \tag{7}$$

where y denotes a distance from the wall, u_τ denotes wall friction velocity and the subscripts i and o denote inner and outer region, respectively. The eddy viscosity in the inner region and the outer region is given, respectively, by

$$\mu_{i,o} = \rho l_{i,o}^2 \left|\frac{\mathrm{d}u}{\mathrm{d}y}\right| \tag{8}$$

2. *Baldwin–Lomax Model*

In the Baldwin–Lomax model [24], the mixing length in the inner region, l_i, is given by Eq. (6). The eddy viscosity in the inner region becomes

$$\mu_i = \rho l_i^2 |\omega| \tag{9}$$

The eddy viscosity in the outer region is

$$\mu_o = \rho\alpha C_{\mathrm{cp}} F_{\mathrm{wake}} F_{\mathrm{Kleb}} \tag{10}$$

where $\alpha = 0.0168$ and $C_{\mathrm{cp}} = 1.6$. The outer function, F_{wake} is given by

$$F_{\mathrm{wake}} = y_{\max} F_{\max} \tag{11}$$

where $F_{\max} = \max(y|\omega|D)$. The Klebanoff intermittency function is

$$F_{\text{Kleb}} = \left[1 + 5.5\left(\frac{C_{\text{Kleb}}y}{y_{\max}}\right)^6\right]^{-1} \tag{12}$$

The turbulent Prandtl number, Pr_t, is used to calculate the turbulent thermal conductivity. In this study, Pr_t is set to a constant value of 0.9, which is widely used for many of high-temperature turbulent flow calculations.

Calculations were carried out for a given mass flow rate and electrical current using the original ARCFLO and Baldwin–Lomax turbulence models to compare the axial velocity and the temperature distributions in the radial direction [25]. From the calculations, it was found out that the eddy viscosities in the outer region calculated by the Baldwin–Lomax model were higher than those by the original ARCFLO model. As a result, the momentum and energy transport in the radial direction calculated by the Baldwin–Lomax model became slightly stronger compared to that by the original ARCFLO model. It was shown that near the centerline, the axial velocity and temperature values calculated by the Baldwin–Lomax model were lower than those obtained by the original ARCFLO model by about 10% for the axial velocity and about 5% for the temperature, respectively. On the other hand, near the wall region, the axial velocity and temperature values calculated by the Baldwin–Lomax model are lower than those by the original ARCFLO model.

D. Other Computational Modeling

The axisymmetric viscous flow is assumed to be in thermochemical equilibrium, because the pressure is typically larger than or the order of 1 atm. Mass, momentum, and energy conservation equations are discretized using a finite-volume method. Joule heating and radiative source terms are included in the right-hand side of the energy equation. Solutions are obtained by numerically integrating the equations in time to steady state. Computed flow properties are second-order accurate in space.

In the arc heaters analyzed in the present study, gas is introduced from the entire length of the constrictor section, the upstream end of the anode chamber, and the cathode chamber. A mixture of argon and air introduced from the walls of the constrictor and the two electrode chambers duplicates the experimental mixture, as was done in our previous work [4]. The value of the mass flow rate from both the anode and cathode chambers is taken as 0.03 kg/s for the AHF and 0.04 kg/s for the IHF, respectively. The remainder of the mass flow rate is injected from the constrictor wall. In a series of IHF experiments considered in the present study, additional air was injected downstream of the cathode chamber and the additional air flow rate was taken to be nominally 0.04 kg/s. A small variation of the additional air flow rate is not expected to affect computed solutions.

The thermochemical state of the injection gas is unknown. In our previous study [19], the temperature of the injection gas was assumed to be same as the wall temperature, and it was set to be either 500 or 1000 K. In reality, however, the injection gas temperature is determined by the details of the flow path from the high-pressure reservoir to the arc heater, and the injection gas temperature is likely to be less than 1000 K. Thus, the temperature of the injection gas is taken to be 300 K and the temperature of the wall to be 1000 K in the present study. However, it should be noted that the computed heat flux values at wall were little changed by the wall and injection gas temperatures assumed [19]. A no-slip boundary condition is imposed at the wall.

The computational procedure in the anode chamber is retained from the work by the present author and his associates [4,19]. In those works, the radius of the anode chamber was taken to be the same as that of the constrictor, although the anode assembly has an inside diameter that is 1.8 times greater than the constrictor. In addition, a constant electrical current distribution is assumed therein. The primary purpose to develop the ARCFLO3 code is to calculate the flow properties in the downstream region of the arc heater. The simplified representation of the anode chamber did not affect the flow properties at the downstream locations [4].

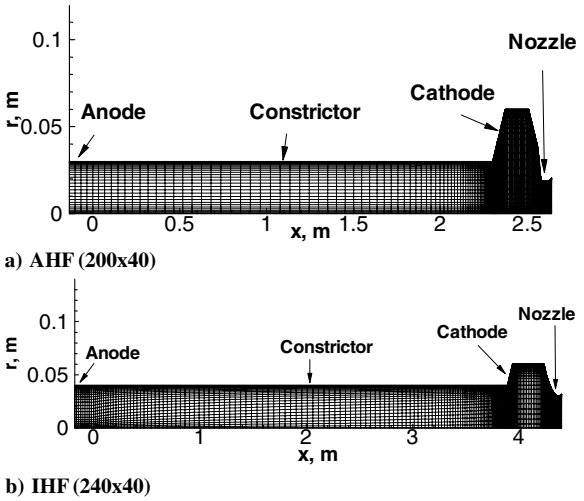

Fig. 4 Computational grid.

The exact distribution of currents in the cathode chamber is not known very well. Two electrical current distributions are tested in the cathode region: one is held constant up to the middle of the cathode, and another is decreased linearly in the cathode as was done in the work of Kim et al. [3]. Calculations are made for the case of $I = 2000$ A by using two current distributions. The results show that the difference of the computed operational characteristic parameters is less than 1% between the two representations of the current distribution in the cathode. Thus, the contribution to the current distributions tested is believed to be negligibly small. In the present study, the constant current distribution is used in the cathode region, just for simplicity. The current distribution in the constrictor is assumed to be constant, which was done in the original ARCFLO code [2].

E. Computational Grid

The AHF arcjet facility has a constrictor diameter of 6 cm and length of 2.3 m. The nozzle throat diameter is 3.8 cm. The computational grid for the AHF facility is shown in Fig. 4a. The radial direction r is magnified by a factor of 10. The entrance of the constrictor is set to be $x = 0$. The grid extends just downstream of the throat to ensure supersonic flow at the exit.

Similarly, the computational grid for the IHF arcjet facility is shown in Fig. 4b. The IHF facility has a constrictor diameter of 8 cm, length of 3.9 m and a nozzle throat diameter of 6.03 cm.

For the PTF arc heater calculations, the AHF computational grid is used because the primary objective for the PTF calculations is to compare the wall heat flux in the constrictor and because, as is shown in Table 1, the PTF constrictor has the same diameter and nearly the same length as that of the AHF except for the nozzle geometry. Although the size of the nozzle throat should affect the upstream chamber pressure, there was a small difference of the chamber pressure between the measurement and calculation.

Calculations were carried out for typical AHF and IHF arc heater conditions using double the number of grid points in the radial direction. The computed operational characteristic values change by about 1%. The refinement in the axial grid resolution changed the computed solutions less than that in the radial direction. These results suggest that grid refinement would not change the overall features of the computed solutions.

III. Results

A. Comparison with PTF Heat Flux Data

Taunk et al. [5] measured the total (convective and radiative) heat flux values at two different locations in the PTF arc heater for several different chamber pressures and electrical currents. Calculations are

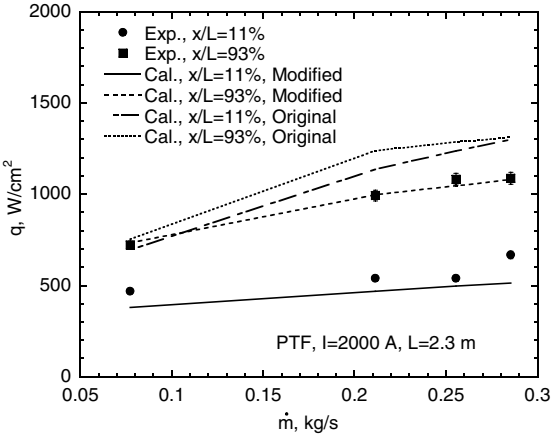

Fig. 5 Comparison of heat fluxes at two different locations in PTF constrictor between different physical models and experiment for $I = 2000$ A; some experimental bars are inside of symbols.

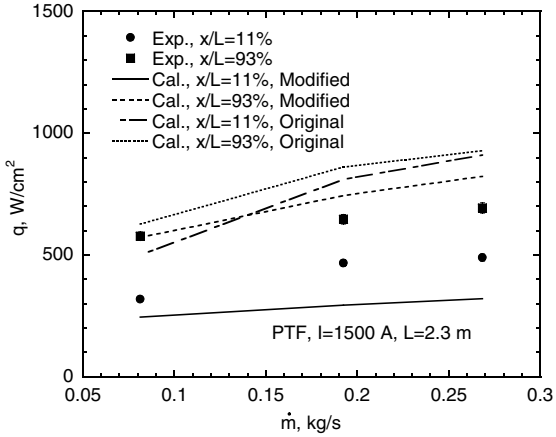

Fig. 6 Comparison of heat fluxes at two different locations in PTF constrictor between different physical models and experiment for $I = 1500$ A; some experimental bars are inside of symbols.

carried out for the electrical current values of $I = 1500$, 2000 and 2300 A.

Figure 5 compares the total heat flux values between the experiment and calculations plotted against mass flow rate for the case of $I = 2000$ A. The heat flux values are given both at an upstream location of about $x/L = 11\%$, and at a downstream location of about $x/L = 93\%$, where L denotes the constrictor length and equals 2.3 m. The computed heat fluxes are obtained by using two different sets of physical models: the one with the two-band radiation model and the original ARCFLO turbulence model (designated as "original"), and another with the three-band radiation and the Baldwin–Lomax turbulence models (designated as "modified"). Between the two sets, the turbulence model used is different. The impact of the turbulence models on the computed heat fluxes is relatively less comparing with that of the radiation model, though the results are not shown. It should be noted that the present result is valid only in comparison between the original ARCFLO and the Baldwin–Lomax turbulence models.

From Fig. 5, at the upstream location of $x/L = 11\%$, the calculated results by the modified method are closer to the experimental data than the original method. Though not shown here, the calculated radiative heat flux is more than 90% of the total heat flux at this upstream location. The calculation by the modified method underestimates the experimental data, with a relative error of 8–17%. The heat flux values calculated by the original method are 50–100% higher than the measurements.

A similar comparison is made in Fig. 5 at a downstream location of $x/L = 93\%$. It is seen that the original method predicts heat fluxes higher than the modified method. The difference between the two methods is relatively smaller than at the upstream location. This result is because, in the downstream location, the radiative heat flux calculated by the original method is still a factor of 2 higher than that calculated by the modified method, but the convective heat flux calculated by the modified method is higher than that calculated by the original method. The modified method gives a good agreement with the measurement.

In Figs. 6 and 7, similar comparisons are shown for the cases of $I = 1500$ and 2300 A, respectively. For the upstream location, one can see that the original method predicts higher heat fluxes than the modified method, in the same way as with the $I = 2000$ A case. The computed heat flux using the modified method approaches the measured value, but still underestimates it by about 30%. From the downstream results, it is seen that the calculation by the original method moderately overestimates the measured heat fluxes. The calculation using the modified method roughly agrees with the measurement, although the modified method tends to slightly overestimate the measurement.

Generally, a fair agreement is seen between the measurement and the calculation using the modified method. In the upstream region, the range of the relative error of 17–130% by the original method is reduced by that of −6 to −40% by the modified method. In the downstream region, the range of 8–28% by the original method is reduced by that of −1 to 19% by the modified method.

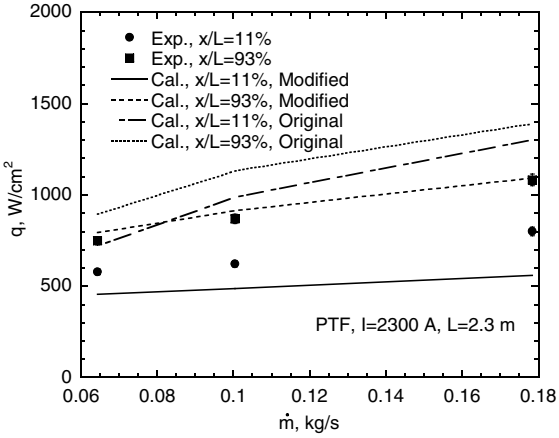

Fig. 7 Comparison of heat fluxes at two different locations in PTF constrictor between different physical models and experiment for $I = 2300$ A; some experimental bars are inside of symbols.

B. Comparison with AHF Data

Recently, a series of arcjet tests were performed in the AHF facility to obtain the mass-averaged enthalpy using the energy balance method [6]. The AHF arcjet was operated over a wide range of mass flow rate and electrical current conditions. Experimental measurements were made of arc current, voltage between electrodes, heater efficiency, chamber pressure, and mass flow rate [6]. Results are presented for the cases of $I = 1600$ and 2000 A. Computations are performed at five mass flow rates that cover the range of the experimental data for each electrical current case. Calculations by using the original method are made for the case of $I = 2000$ A for the purpose of comparison.

Figures 8a and 8b show the voltage between the electrodes for the cases of $I = 1600$ and 2000 A, respectively. The data are plotted against mass flow rate. The computed voltage increases with mass flow rate. The qualitative trend of the calculated results is similar to that of the experiment. From Fig. 8a, a fair agreement is seen between the calculation and the measurement, though the calculation overestimates the measured voltage values by up to about 30%. From Fig. 8b, it is seen that the computed voltages by the modified method are slightly lower than those by the original method. Both computations give a better agreement with the measurement only in the higher mass flow rate range. Except of that range, the

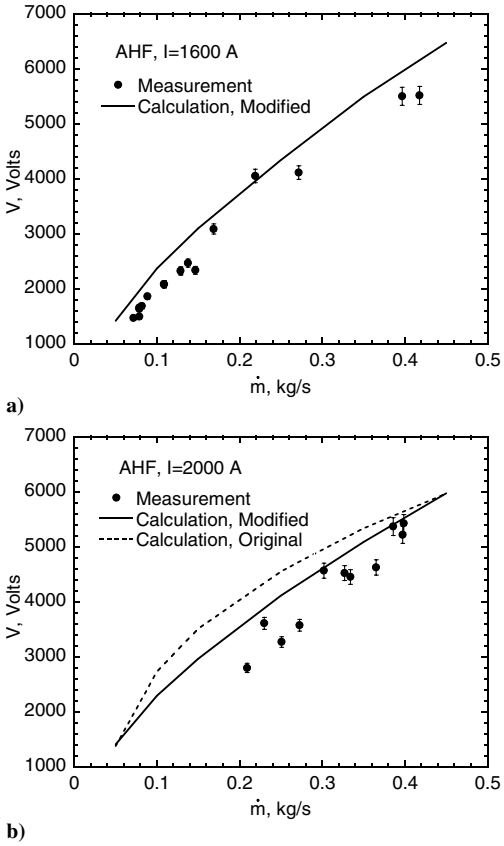

Fig. 8 Comparison of voltage between calculation and experiment for AHF operating conditions; some experimental bars are inside of symbols.

computation overestimates the measurement by 25–35% at mass flow rates between 0.2 and 0.3 kg/s.

In Figs. 9a and 9b, the computed and measured heater thermal efficiencies are compared. The computed efficiency, η, is given by

$$\eta = 1 - \frac{\text{Heat loss from the wall}}{\text{Net power input}}$$

The power input to the gas from the Joule heating is calculated using $I \times V$. In addition, there is a small heat input due to the injection of the gas from the wall. The net power input is given by the sum of these two contributions. The heat loss from the wall is obtained by integrating the heat flux at the wall from the upstream end of the anode chamber to the nozzle throat. The heat loss in the downstream region of the nozzle beyond the throat is not included in the calculation. Experimentally, the heat transfer to the wall is measured up to the end of the nozzle. Based on the analysis by Winovich [26], we estimated that the heat loss in the diverging section of the nozzle beyond the throat would be about 1%. Therefore, the contribution to the computed efficiency from the downstream region beyond the throat is considered to be negligibly small. In both figures, it can be seen that the computed efficiency increases with mass flow rate. From Fig. 9a for $I = 1600$ A, the computation predicts the efficiency within the scatter of the experiment in the lower mass flow rate range. However, the computed values become higher than the measured ones in the higher mass flow rate range. In Fig. 9b for $I = 2000$ A, the computed efficiency by the modified method is higher than that by the original method. The computation by the modified method is 10–30% higher than the experiment for the mass flow rates considered. The computation by the original method is 10–30% lower than the experiment.

Figure 10 shows the comparison of the mass-averaged enthalpy between the experiment and calculations for the two electrical current cases. The computed mass-averaged enthalpy is evaluated by integrating the flow properties at the nozzle throat:

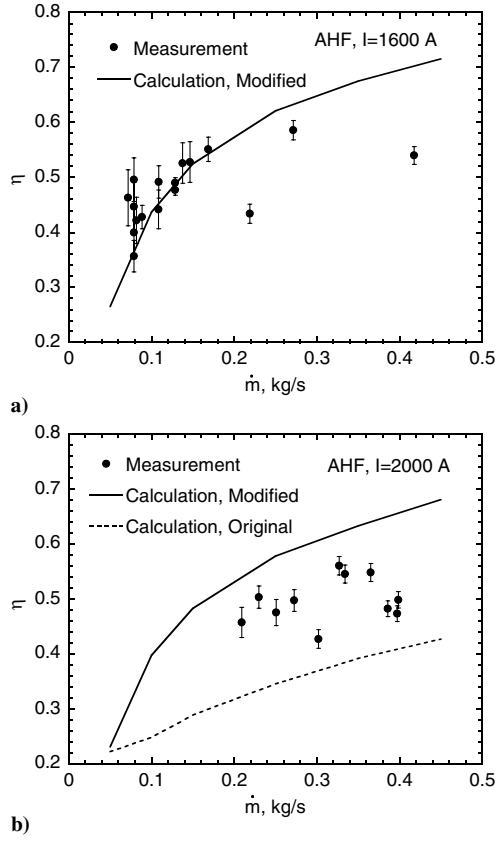

Fig. 9 Comparison of efficiency between calculation and experiment for AHF operating conditions.

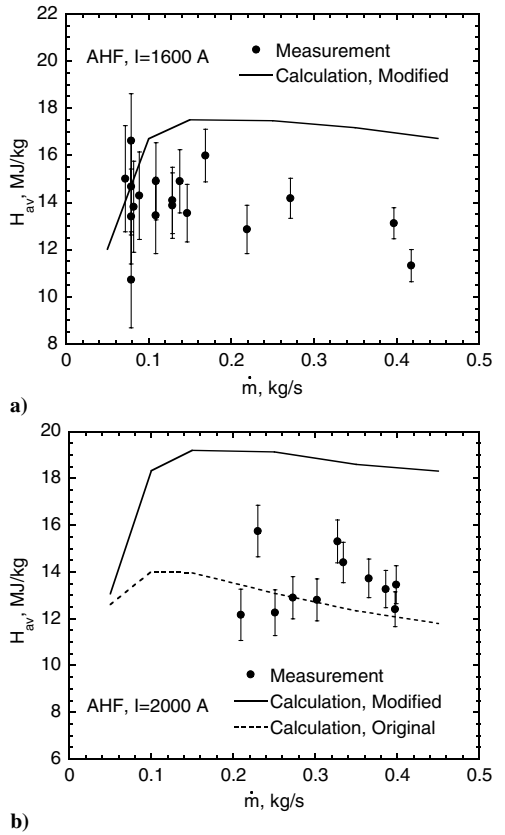

Fig. 10 Comparison of mass-averaged enthalpy between calculation and experiment for AHF operating conditions.

$$H_{\text{av}} = \frac{\int_0^R \rho u H r \, \mathrm{d}r}{\int_0^R \rho u r \, \mathrm{d}r} \tag{13}$$

One can also obtain the computed mass-averaged enthalpy using the energy balance between the net heat input and the heat loss from the wall:

$$H_{\text{av}} = \frac{I \times V}{\dot{m}} \times \eta \tag{14}$$

These two values should be the same if energy conservation holds. In all calculations, the difference of the two values is less than about 1%. From Fig. 10, the computed mass-averaged enthalpy has a peak at a mass flow rate of about 0.15 kg/s. For higher mass flow rates beyond this peak point, the computed mass-averaged enthalpy decreases. A reasonable agreement is seen in Fig. 10a for $I = 1600$ A at the lower mass flow rates, but the computation predicts slightly higher enthalpies at the higher mass flow rates as compared to the measurements. The results are consistent with the efficiency comparisons seen in Fig. 9a. For $I = 2000$ A, Fig. 10b shows that the computations by the modified method overestimate the experimental data by about 10–30% for all mass flow rates. The computation by the original method gives a better agreement with the measurement than the modified method. However, it is noted that this agreement between the original method and measurement is coincidence, which comes from two facts: the larger heat input indicated by Fig. 8b and the lower efficiency shown in Fig. 9b.

A similar comparison is made for chamber pressure and the results are shown in Fig. 11. As can be seen in Fig. 11a, the difference between the experiment and calculation becomes larger as the mass flow rate increases. For $I = 2000$ A, Fig. 11b shows that the computation by the modified method overestimates the measurements by 30% over all the mass flow rates considered. Although the computation by the original method also gives higher chamber pressures as compared to the measurement, the results by the original method are closer to the measurements than those by the modified method.

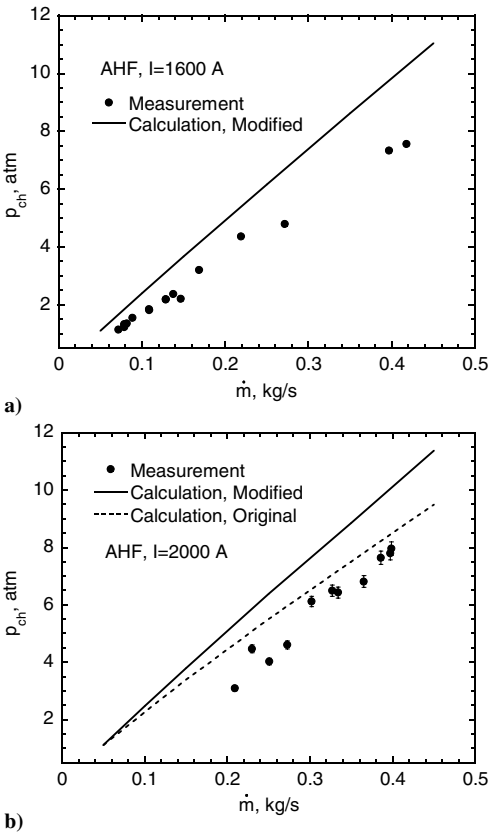

Fig. 11 Comparison of chamber pressure between calculation and experiment for AHF operating conditions; some experimental bars are inside of symbols.

C. Comparison with IHF Data

A series of arcjet tests have been performed recently in the IHF facility.[†] Similar comparisons to those shown in the preceding section are made for the IHF experimental data for the electrical current values of $I = 3000$ and 6000 A. Calculations are carried out at four different mass flow rates for each electrical current case. For the purpose of comparison, the computations by the original method are performed for the case of $I = 3000$ A.

The computed results are summarized in Figs. 12–15 for voltage, efficiency, mass-averaged enthalpy, and chamber pressure. Comparing the results for the original method and the modified method for the case of $I = 3000$ A, the modified method predicts

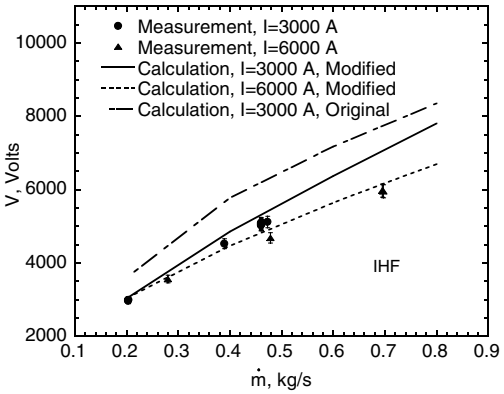

Fig. 12 Comparison of voltage between calculation and experiment for IHF operating conditions.

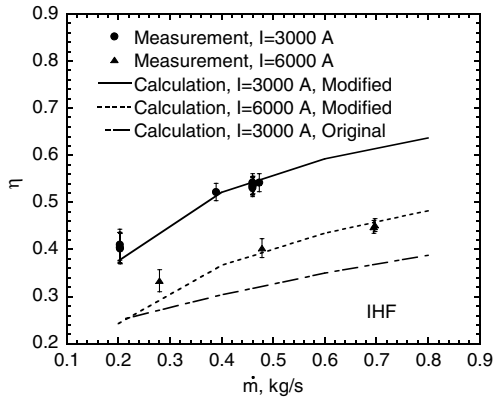

Fig. 13 Comparison of efficiency between calculation and experiment for IHF operating conditions.

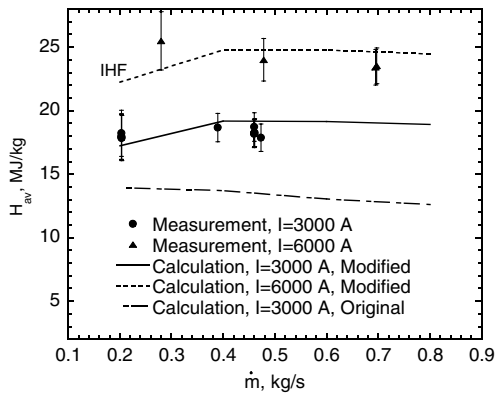

Fig. 14 Comparison of mass-averaged enthalpy between calculation and experiment for IHF operating conditions.

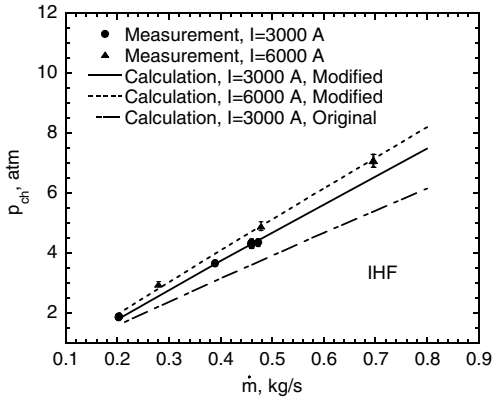

Fig. 15 Comparison of chamber pressure between calculation and experiment for IHF operating conditions; some experimental bars are inside of symbols.

lower voltages and higher heater efficiency, mass-averaged enthalpy, and chamber pressure than the original method, as is seen in the results for AHF. Unlike the case for AHF, calculated values by the modified method are in good agreement with experimental data for both electrical current values. The original method fails to reproduce any of the data.

Figure 12 shows that the computed voltage is weakly affected by changing electrical current. The net power input in the arc heater for $I = 6000$ A is nearly twice that of $I = 3000$ A. However, as is seen from Fig. 13, the heater efficiency decreases as the electrical current increases. As a result, Fig. 14 shows that the mass-averaged enthalpy for $I = 6000$ A is only 40% greater than the mass-averaged enthalpy for $I = 3000$ A. Though the results are not shown here, the total heat loss from the wall for $I = 6000$ A becomes larger than that for $I = 3000$ A by a factor of 2.5 for the same mass flow rate. Also, the heat loss by radiation for $I = 6000$ A becomes about 60% of the total heat loss, and about 40% for $I = 3000$ A for the mass flow rates calculated in the present study. As seen from Fig. 15, the computed chamber pressure increases about 10% for all mass flow rates considered as the electrical current increases.

D. Comparisons with Fletcher and Bamford's LIF Data in AHF [7]

In Fig. 16, the centerline enthalpy calculated using the modified method is compared with the measurement. The calculated enthalpy at the centerline was evaluated at the nozzle throat. The data are plotted against electrical current. The results are shown for two types of operating conditions: one is the low electrical current and low mass flow rate (0.11 kg/s) and another is the high electrical current and high mass flow rate (0.2 kg/s). In the figure, the calculated mass-averaged enthalpy was also shown for the purpose of comparison. At the time of the Fletcher and Bamford's experiments [7], the

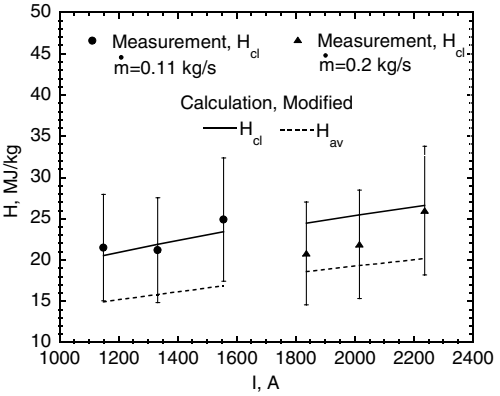

Fig. 16 Comparison of enthalpy at centerline between calculation and Fletcher et al.'s experiment [7].

Table 2 Comparison of voltage, chamber pressure, heater efficiency, mass-averaged enthalpy, and centerline enthalpy between the present calculation and Park et al.'s experiment [8]

	V, V	p_{ch}, atm	η	H_{av}, MJ/kg	H_{cl}, MJ/kg
Experiment	4828	4.47	0.40	28.7	40.6
Calculation	4767	4.37	0.38	27.1	37.6

instrumentation necessary for mass-averaged enthalpy was not installed, and therefore the measured value does not exit.

From Fig. 16, a fair agreement is seen between the measurement and calculation for the case of the low electrical current and low mass flow rate. On the other hand, for the case of the higher electrical current, the calculation tends to overestimate the measurement by up to 40%, although the calculated results are within the error bar for the measurement. It is noted that the computed mass-averaged enthalpy values were in a fair agreement with the measurement for lower mass flow rate, but for higher mass flow rate, the computed mass-averaged enthalpies were larger than the measured ones. Thus, the results seen in Fig. 16 are consistent with the mass-averaged enthalpy comparisons seen in Fig. 10.

From the calculations, it is found that the ratio of the computed centerline enthalpy to the mass-averaged enthalpy is about 1.4 for the case of the low mass flow rate, and is about 1.33 for the case of the high mass flow rate. For the calculated results for the AHF data shown in the preceding section, the ratio varies roughly from 1.5 to 1.3 for both of electrical current values as the mass flow rate increases.

E. Comparisons with Park et al.'s Spectroscopic Data in IHF [8]

In the Park et al. IHF experiment [8], the radiation emanated from the shock layer over a blunt model was measured. The centerline enthalpy was deduced by replicating the measured spectra using theoretical methods. Calculation is made for the case of the electrical current of 6066 A and the mass flow rate of 0.412 kg/s taken from that experiment. The computed voltage, chamber pressure, heater thermal efficiency, mass-averaged enthalpy, and centerline enthalpy are summarized in Table 2. As expected, the computed values of voltage, chamber pressure, thermal efficiency, and mass-averaged enthalpy are in a good agreement with the measurement, as was seen in the preceding section. The centerline enthalpy obtained by the spectroscopic method was 40.6 MJ/kg, and the value of the computed centerline enthalpy was 37.6 MJ/kg. The computed value is slightly lower than the measurement by about 7%, which is within the standard deviation of 10% reported by Park et al. [8].

For the IHF arc heater conditions calculated in the previous section, the ratio of the centerline enthalpy value to the mass-averaged value varies from 1.7 to 1.4 for the case of $I = 3000$ A and from 1.5 to 1.4 for the case of $I = 6000$ A, respectively, as mass flow rate increases.

Though the results are not shown here, the computed centerline enthalpies calculated using the original ARCFLO turbulence model are higher than those calculated by the Baldwin–Lomax turbulence model by about 10% when using the three-band radiation model. As a result, the calculation using the original ARCFLO turbulence model leads to higher centerline enthalpy values compared to the measurement.

IV. Discussion

The present results show that the computed solutions are very sensitive to radiation modeling. The observed agreement between the experiment and calculation for the IHF and a part of AHF arc heater conditions indicates that improvement of the radiation and turbulent models made in the present study are essential for the calculation of the arc heater flowfield. One can obtain the freestream properties at the downstream of a nozzle fully theoretically by combining the ARCFLO3 code with a nonequilibrium nozzle flow code. In addition, by obtaining the enthalpy and the pressure of the

freestream, an arc heater operating condition can be related to the flight conditions.

The results for the PTF and AHF arc heater conditions show that by incorporating more rigorous physical models, the calculated data approach the experiments. However, there is still a relatively poor agreement between the experiment and calculation for a part of the AHF data, particularly in the data of chamber pressure and heater efficiency. Several physical assumptions were examined as possible sources of the discrepancy, especially for wall boundary treatment including roughness [19]. The results showed that these assumptions had only small contribution to computed solutions.

A possible cause for the discrepancy may be due to neglecting more detailed physics such as thermochemical nonequilibrium effect [27], and three-dimensional flow motion with turbulent swirl flow effect, and electromagnetic hydrodynamic effect, which will occur in the arc heater. As for the heat flux, if atomic species exists in the vicinity of the wall due to chemical nonequilibrium, the catalytic recombination could increase the convective heat flux at the surface. The radiative heat flux at the wall could be changed by possible thermal nonequilibrium. Generally, electron temperature is different from heavy particle temperature in the wall region within the arc heater flowfield. The chamber pressure is believed to be also affected by the thermochemical nonequilibrium effect. As the flow recombines toward the throat, the chemical energy is transferred to the kinetic energy of the flow. The phenomenon tends to raise the pressure. The pressure will be increased less if the flow recombines incompletely. In addition, because an arc foot is rotating by imposing a magnetic field in the cathode chamber, the flow is swirling [28]. The swirling flowfield in the cathode region could also change the flow state at the nozzle throat. Whether such more detailed modeling could explain the discrepancy seen in the present study remains to be investigated in the future.

V. Conclusions

The high enthalpy flows in high-power arc heaters at NASA Ames were simulated using the computational fluid dynamics code named ARCFLO3. The computed results were compared with the measurement for arc voltage between electrodes, chamber pressure, and heater thermal efficiency. By using a newly developed three-band radiation model and the Baldwin–Lomax turbulence model, a better agreement is obtained between the calculation and measurement for a broader range of operational conditions. Thus, the modified ARCFLO3 code gives an increased confidence for the calculation of the arc heater flowfield. A poor agreement, as is seen between the calculation and the measurement for a certain range of operating conditions in AHF, is still an unresolved issue. To improve current computational capabilities to characterize the arcjet flow, more work needs to be done.

Acknowledgments

Most of this work have been done while the present author was a National Research Council associate at NASA Ames. The author would like to thank Joseph Olejniczak (NASA Ames), Chul Park (ELORET, currently at Korean Advanced Institute of Science and Technology), for their encouragement and technical guidance throughout this work. The author would also like to thank T. Mark Hightower (NASA Ames), Jaswinder Taunk (ELORET), and John Balboni (NASA Ames), for providing the experimental data and helpful suggestions.

References

[1] Balter-Peterson, A., Nichols, F., Mifsud, B., and Love, W., "Arc Jet Testing in NASA Ames Research Center Thermophysics Facilities," AIAA Paper 92-5041, Dec. 1992.

[2] Nicolet, W. E., Shepard, C. E., Clark, K. C., Balakrishnan, A., Kesselring, J. P., Suchsland, K. E., and Reese, J. J., "Analytical and Design Study for a High-Pressure, High-Enthalpy Constricted Arc Heater," AEDC TR-75-74, July 1975.

[3] Kim, K. H., Rho, O. H., and Park, C., "Computation of Arc-Heated Flows Using a Navier-Stokes Code," *Journal of Thermophysics and Heat Transfer*, Vol. 14, No. 2, 2000, pp. 280–258.

[4] Sakai, T., and Olejniczak, J., "Navier-Stokes Computations for Arcjet Flows," AIAA Paper 2001-3014, June 2001.

[5] Taunk, J. S., Shepard, C. E., and Carraso, A., "Design and Verification of a Copper Disk for Radiation Measurements in the Constrictor Region of an Arc Jet," Instrument Society of America Paper 94-3025, Baltimore, MD, 1994.

[6] Hightower, T. M., Balboni, J. A., MacDonald, C. L., Anderson, K. F., and Martinez, E. R., "Enthalpy by Energy Balance for Aerodynamic Heating Facility at NASA Ames Research Center Arc Jet Complex," *Proceedings of the 48th International Instrumentation Symposium* [CD-ROM], Vol. 420, Instrumentation, Systems, and Automation Society, San Diego, CA, 2002.

[7] Fletcher, D. G., and Bamford, D. J., "Arcjet Flow Characterization Using Laser-Induced Fluorescence of Atomic Species," AIAA Paper 98-2458, June 1998.

[8] Park, C., Raiche, D. M., Driver, D. M., Olejniczak, J., Terrazas-Salinas, I., Hightower, T. M., and Sakai, T., "Comparison of Enthalpy Determination Methods for an Arc-Jet Facility," AIAA Paper 2004-487, Jan. 2004.

[9] Milos, F. S., "ARCFLO Analysis for High-Enthalpy Arc Heaters," AIAA Paper 91-1384, June 1991.

[10] Park, C., "Nonequilibrium Air Radiation (NEQAIR) Program: User's Manual," NASA TM 86707, July 1985.

[11] Sakai, T., Sawada, K., and Mitsuda, M., "Application of Planck-Rosseland-Gray Model for High Enthalpy Arc Heaters," *Journal of Thermophysics and Heat Transfer*, Vol. 15, No. 2, April–June 2001, pp. 176–183.

[12] Matsuyama, S., Sakai, T., Sasoh, S., and Sawada, K., "Parallel Computation of Fully Coupled Hypersonic Radiating Flowfield Using Multiband Model," *Journal of Thermophysics and Heat Transfer*, Vol. 17, No. 1, Jan.–March 2003, pp. 21–28.

[13] Sakai, T., Sawada, K., and Park, C., "Assessment of Planck-Rosseland-Gray Model for Radiating Shock Layer," AIAA Paper 97-2560, June 1997.

[14] Vincenti, W. G., and Kruger, C. H., *Introduction to Physical Gas Dynamics*, John Wiley & Sons, New York, 1965, pp. 473–522.

[15] Whiting, E. E., Park, C., Liu, Y., Arnold, J. O., and Paterson, J. A., "NEQAIR96, Nonequilibrium and Equilibrium Radiative Transport and Spectra Program: Users Manual," NASA Reference Publication 1389, Dec. 1996.

[16] Gupta, R. N., Yos, J. M., Thompson, R. A., and Lee, K., "A Review of Reaction Rates and Thermodynamic and Transport Properties for an 11-Species Air Model for Chemical and Thermal Nonequilibrium Calculations to 30,000 K," NASA RP 1232, 1990.

[17] Partridge, H., Stallcop, J. R., and Levin, E., "Potential Energy Curves and Transport Properties for the Interaction of He with Other Ground-State Atoms," *Journal of Chemical Physics*, Vol. 114, No. 14, 2001, pp. 6471–6488.

[18] Devoto, R. S., "Transport Coefficients of Ionized Argon," *The Physics of Fluids*, Vol. 16, No. 5, 1973, pp. 616–623.

[19] Sakai, T., and Olejniczak, J., "Improvements in a Navier-Stokes Code for Arc Heater Flows," AIAA Paper 2003-3782, June 2003.

[20] Thomas, L. D., and Nesbet, R. K., "Low-Energy Electron Scattering by Atomic Oxygen," *Physical Review A*, Vol. 11, No. 1, 1975, pp. 170–173.

[21] Thomas, L. D., and Nesbet, R. K., "Addendum: Low-Energy Electron Scattering by Atomic Oxygen," *Physical Review A*, Vol. 12, No. 4, 1975, pp. 1729–1730.

[22] Thomas, L. D., and Nesbet, R. K., "Low-Energy Electron Scattering by Atomic Nitrogen," *Physical Review A*, Vol. 12, No. 6, 1975, pp. 2369–2377.

[23] Blaha, M., and Davis, J., "Elastic Scattering of Electrons by Oxygen and Nitrogen at Intermediate Energies," *Physical Review A*, Vol. 12, No. 6, 1975, pp. 2319–2324.

[24] Baldwin, B., and Lomax, H., "Thin-Layer Approximation and Algebraic Model for Separated Turbulent Flows," AIAA Paper 78-0257, Jan. 1978.

[25] Sakai, T., "Computational Simulation of High Enthalpy Arc Heater Flows," AIAA Paper 2006-1183, Jan. 2006.

[26] Winovich, W., "On the Equilibrium Sonic-Flow Method for Evaluating Electric-Arc Air-Heater Performance," NASA TN D-2132, March 1964.

[27] Sharma, P. S., Park, C. C., Scott, C. D., Arepalli, S., and Taunk, J., "Arcjet Flow Characterization," AIAA Paper 96-0612, Jan. 1996.

[28] Durgapal, P., "Current Distribution in the Cathode Area of an Arcjet," *Journal of Thermophysics and Heat Transfer*, Vol. 7, No. 2, April–June 1993, pp. 241–250.